

Effects of Grain Boundary Misorientation on Radiation-Induced Solute Segregation in Proton Irradiated 304 Stainless Steels

Ji Jung Kai¹, Fu Rong Chen¹ and Ting Shien Duh²

¹Center for Electron Microscopy, Department of Engineering and System Science, National Tsing Hua Univ., Hsinchu, Taiwan 30043, R.O.China

²Institute of Nuclear Energy Research, AEC, Lungtan, Taoyuan, 325, Taiwan, R.O.China

This paper describes the effects of the grain boundary misorientation on the radiation induced segregation (RIS) in proton irradiated 304 stainless steels. Experimentally, four test conditions were used for the 304 stainless steel specimens: (1) As-received (AR) with enriched Cr at grain boundary, (2) AR + 1 dpa proton irradiated at 450°C, (3) Thermal sensitized (SEN), and (4) SEN + 1 dpa proton irradiated at 450°C. Compared with no pre-enrichment condition, a delayed Cr depletion was found at grain boundaries in AR + 1 dpa specimens. After irradiation, the Cr concentration profile across grain boundaries became narrower and deeper in SEN + 1 dpa specimens. The degree of grain boundary segregation was observed to be higher at random boundaries than special boundaries. In the case of SEN + 1 dpa specimens, the segregation cusps were observed at grain boundaries of $\Sigma 3$, $\Sigma 9$ and $\Sigma 15$, and the Cr segregation levels at special boundaries were increasing with Σ for value up to $\Sigma = 15$. Theoretically, a simple rate equation model with modified boundary conditions, which were related to the grain boundary diffusion of defects and the densities of the grain boundary dislocations, was developed for RIS at boundaries with different Σ and $\Delta\theta$. The model calculations showed that the RIS model with modified boundary conditions could predict clearly the same trend as that of experiments, in which the Cr depletion levels at special boundaries in irradiated 304 stainless steels were increasing with Σ . The model calculations also showed that the widths of the segregation cusps were decreasing with increasing Σ .

(Received September 3, 2003; Accepted October 27, 2003)

Keywords: grain boundaries, radiation-induced segregation, proton irradiation, radiation effects, theoretical modeling, austenitic stainless steels

1. Introduction

It is well known that Cr depletion near grain boundaries is a major factor causing the IASCC⁽¹⁾ and IGSCC in irradiated and thermal sensitized austenitic stainless steels, respectively. The mechanisms of these two grain boundary segregation phenomena are different. The thermal sensitization effect is driven by thermodynamic forces. In contrast, RIS is a non-equilibrium effect and is driven by kinetic processes.⁽²⁾ The Cr depletion during thermal sensitization is caused by the diffusion of Cr and Carbon to grain boundaries and forming Cr carbide at the grain boundaries. The mechanisms of the radiation-induced solute segregation (RIS) may be described by inverse-Kirkendall models.⁽³⁾

Many studies have indicated that the grain boundary related properties, such as grain boundary energy,⁽⁴⁾ grain boundary migration,⁽⁵⁾ grain boundary diffusion,⁽⁶⁾ and grain boundary segregation are dependent upon the grain boundary structure. For grain boundary segregation,⁽⁷⁾ small angle boundaries generally exhibit smaller amounts of segregation than large angle boundaries. For large angle boundaries, the variations in segregation to most general boundaries may be up to $\pm 30\%$ of the average in polycrystalline specimens,⁽⁸⁾ the strength of the segregation at grain boundary depends on the structure of the grain boundary. In general, the high energy grain boundaries have more preferential sites for solute segregation than low energy boundaries such as CSL (Coincidence Site Lattice) grain boundaries, especially $\Sigma 3$ twin boundaries. Therefore, it is reasonable to propose that grain boundary structure may be an important factor which would affect the degree of RIS at grain boundary.

The effects of grain boundary structure on grain boundary segregation have been studied by many workers^(7,9,10) in the

past years. However, the effects of grain boundary structure on radiation induced segregation (RIS) has not been investigated extensively. In this paper we are interested in the effects of grain boundary misorientation on RIS in proton irradiated 304 stainless steels.

In conventional RIS model, it is generally assumed that the grain boundaries are perfect sinks, and therefore the boundary condition for defect concentrations at the grain boundaries may be taken as equal to the thermal equilibrium defect concentrations. However, in real situation, the actual boundaries, for instance the $\Sigma = 3$ boundaries, would not always behave like perfect sinks.⁽¹¹⁾ The defect concentrations at the grain boundaries will generally depend both upon how rapidly the flux of defects can be absorbed at the boundaries and how fast the flux of defects can diffuse to the grain boundaries.

It is well known that the interfaces can be modeled by continuously or discretely distributed arrays of dislocations.^(12,13) For low-angle boundaries the mechanism available for the absorption of the point defects is the climbing of the primary dislocations in the boundaries. The point defects are absorbed at jogs on the climbing dislocations by means of thermally activated fluctuations.⁽¹⁴⁾ However, for singular or vicinal high-angle boundaries, the absorption of the point defects at boundaries is more readily via the climb of the secondary dislocations,⁽¹⁵⁾ due to the facts that such boundaries with reference structures of low energy are resistant to the simultaneous climb of their primary dislocations. Normally, most of the diffusing defects from the bulk would impinge upon the boundary surface and then diffuse along the grain boundary to the grain boundary dislocations, and furthermore, diffuse along the cores of grain boundary dislocations to the jogs where the defects absorbed.⁽¹⁶⁾

In this paper, the effects of the grain boundary misorientation on the radiation induced segregation in proton irradiated 304 stainless steels will be described and most of them will be referred to our previous works^{11,17,18)} which include both experiments and model calculations.

2. Experiments

2.1 Materials and heat treatments

The composition of the 304SS used in this work is (in mass%): Cr(18.04), Ni(8.23), Mn(1.49), Mo(0.036), P(0.025), S(0.002), Si(0.5), N(0.056), C(0.047) and Fe(bal.). There are two initial conditions, as-received and sensitized, for the irradiated 304SS specimens, therefore we have 4 different conditions for the specimens: As-received (AR), Irradiated (AR + 1 dpa), Sensitized (SEN) and Irradiated-Sensitized (SEN + 1 dpa). The heat treatment for sensitization was carried out at 650°C for 100 hours and then cooled by a water quench, and for the AR specimens the heat treatment was at 1100°C for 3 minutes and cooled by a water quench.

2.2 Proton irradiation

The irradiation tests were performed using a Tandem linear accelerator to promote the RIS effect in both the AR and SEN 304SS specimens. The specimens were irradiated by 5 MeV protons at 450°C to a total dose of 1 dpa. The damage rate was estimated at about 1×10^{-6} dpa/s at the examined region. After irradiation, both the SEN and AR samples were made into TEM specimens of 3 mm diameter and 80-90 μm thick and then prepared by electropolishing for TEM observations.

2.3 FEGTEM/EDS observations

The observations of grain boundary segregation and grain boundary misorientation were performed on JEOL JEM-2010F TEM with X-ray spectrometer attached to the stage. This instrument provides an acceleration voltage of 200 kV and has a small beam size of 0.5 nm. The Cr/Ni-concentration profiles near the grain boundaries were measured by X-ray energy dispersive spectrometry (XEDS) and the grain boundary misorientations were observed by diffraction patterns with Kikuchi maps. The specimens were sputtered with Ar-ions to clean the surface before EDS measurements. The thickness of the examined area in specimen is about 80–100 nm. The X-ray spectra profiles across grain boundaries were taken normally at $\pm 0, 2, 4, 10, 20, 50, 70$ nm steps, and the spectra were taken along the grain boundaries for a minimum of 5 measurements (>5 nm apart) on each edge-on grain boundary. Each X-ray spectra data was collected for 90 seconds with the beam probe checked and repositioned every 30 seconds to keep the drift less than 2 nm.

2.4 Determination of grain boundary misorientation by Kikuchi patterns

The grain boundary misorientation was determined both by measured and simulated Kikuchi patterns. To determine the grain boundary misorientation, first we need to know the beam direction in each grain on both sides of the boundary. A detailed procedure for determining the beam direction in

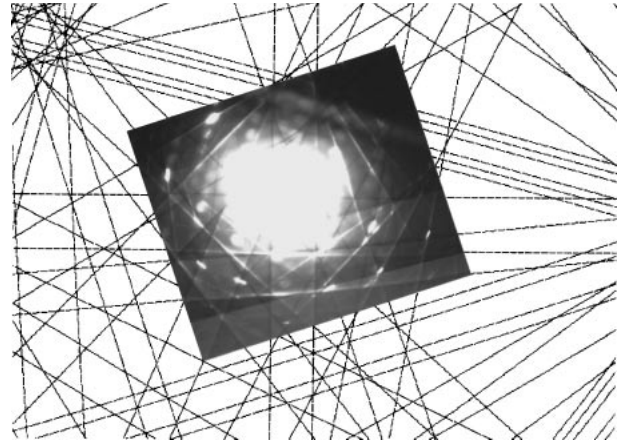


Fig. 1 A good match between the measured and simulated Kikuchi patterns. The measured Kikuchi pattern is shown in the central part.

grains from Kikuchi patterns has been given by Chen and King.¹⁹⁾ The beam direction in crystal is defined to be antiparallel to the direction of electron flow. It is possible to locate the beam spot precisely in a simulated Kikuchi pattern, as shown in Fig. 1. The picture of the Kikuchi pattern in the central part of the Fig. 1 was taken on TEM. As can be seen, we may have a good match between the measured and simulated Kikuchi patterns.

The exact beam direction in each grain can then be determined by solving the relationships of beam direction \mathbf{B}_0 and at least three known pole directions on a simulated Kikuchi pattern \mathbf{P}_1 , \mathbf{P}_2 and \mathbf{P}_3 (see Fig. 2):

$$\cos(x_1/L) = \mathbf{B}_0 \cdot \mathbf{P}_1 / |\mathbf{B}_0| |\mathbf{P}_1|$$

$$\cos(x_2/L) = \mathbf{B}_0 \cdot \mathbf{P}_2 / |\mathbf{B}_0| |\mathbf{P}_2|$$

$$\cos(x_3/L) = \mathbf{B}_0 \cdot \mathbf{P}_3 / |\mathbf{B}_0| |\mathbf{P}_3|$$

where x_1 , x_2 , and x_3 are the distances from beam spot in the

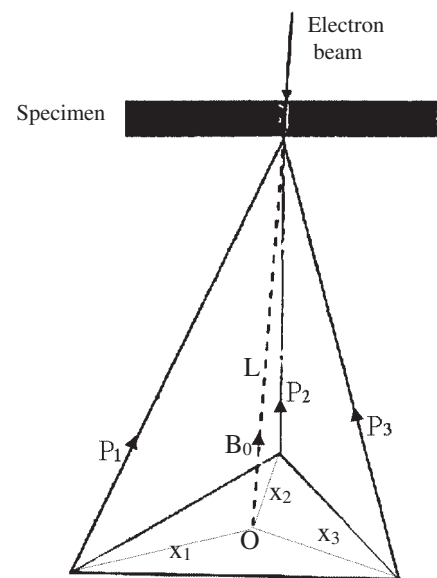


Fig. 2 Schematic diagram to determine the beam direction (\mathbf{B}_0) on a simulated Kikuchi pattern. The distances from beam spot to three known poles \mathbf{P}_1 , \mathbf{P}_2 and \mathbf{P}_3 in the simulated Kikuchi pattern are x_1 , x_2 and x_3 , respectively, and L is the camera length, provided that x/L is very small.

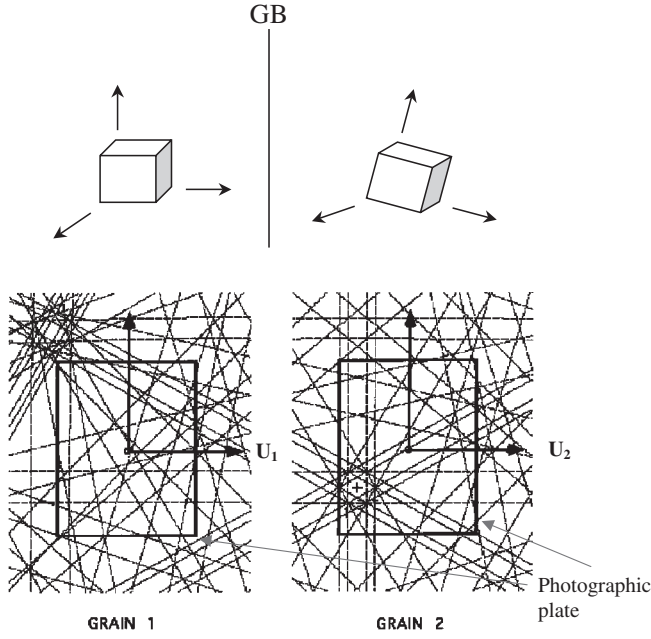


Fig. 3 A pair of Kikuchi patterns with photographic plate attached. The Lab. frame on the plate can be expressed in terms of coordinates of grain 1 and 2 and is denoted as U_1 and U_2 , respectively. U_1 and U_2 are relating by misorientation matrix R , $RU_1 = U_2$.

simulated Kikuchi pattern to three known poles, respectively, and L is the camera length, provided that x/L is very small.

Next, in order to determine the misorientation between two grains, the Lab. frame is considered attached to the photographic plate (with the emulsion side up). The beam direction is taken as z -axis, and the plane on the photographic plate as x - y plane. The Lab. frame can be treated as fixed in space due to the fact that the position of the photographic plate in TEM is fixed. With the known beam direction and Kikuchi pattern, we can express the Lab. frame on photographic plate in terms of the grain coordinate system which may be set up from the simulated Kikuchi patterns. As shown in Fig. 3, the Lab. frame in terms of coordinates of grain 1 and 2 is denoted as U_1 and U_2 , respectively. The misorientation matrix R relating the two grains can be written as:

$$RU_{1i} = U_{2i}, \quad i = x, y \text{ and } z$$

$$R_{ij} = U_{2i} \cdot U_{1j}^{-1}$$

where R is a 3×3 matrix, R_{ij} is the element of matrix R , and U_{1i} and U_{2i} are column vectors. The orientation relationship between two grains can be described by a rotation about an axis. The rotation axis is given by the unit vector parallel to

$$[R_{32} - R_{23}, R_{13} - R_{31}, R_{21} - R_{12}]$$

and the rotation angle θ by

$$\theta = \cos^{-1}((R_{11} + R_{22} + R_{33} - 1)/2)$$

With the rotation axis and angle, the corresponding Σ value can be found from the table made by Mykura in which they listed values of rotation axis and angle for CSL's up to $\Sigma 101$.²⁰⁾

In general, the measured grain boundaries are not exact CSL boundaries. The total deviations from exact CSL, $\Delta\theta$, may come from the deviations in both the misorientation axis

and the angular misorientation. Hence, $\Delta\theta$ is defined as the averaged angular difference between the column vectors of the CSL misorientation matrix and the respective column vectors of the measured misorientation matrix.²¹⁾ The permissible deviation from an exact CSL can be determined by the Brandon criterion.²²⁾ In this paper, we label a boundary by the nearest Σ , although it may have been over the permissible deviation from a CSL boundary of Σ . The lowest-angle/axis pair will be used here to denote the misorientation relationship between 2 adjoining grains.

3. Experimental Results

3.1 AR and AR + 1 dpa specimens

Figure 4 shows the Cr concentration profiles across grain boundaries of different Σ value in the as-received 304SS specimens. The Cr enrichment is observed near grain boundaries and the degree of Cr enrichment is different from boundary to boundary for the AR specimens. We can see from Fig. 4 that the majority of the enriched Cr atoms at grain boundaries typically lie in a narrow zone of 3-4 nm. The segregation levels of Cr atoms ($\Delta Cr \equiv Cr_{gb} - Cr_{matrix}$) at boundaries of different Σ value are shown in Fig. 5 for both AR and AR + 1 dpa specimens. All the boundaries in Fig. 5 (and the following figures) are not exact CSL boundaries, rather they have deviations from CSL structures. Here, we

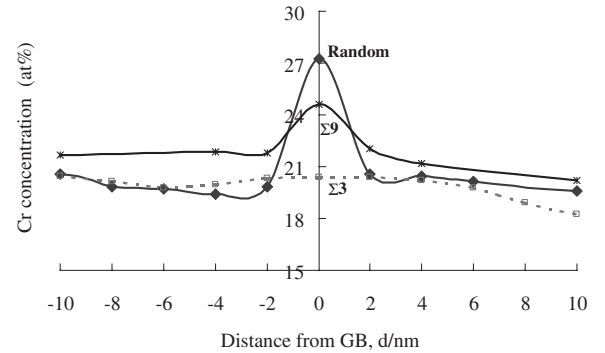


Fig. 4 The Cr concentration profiles across grain boundaries of different Σ value in the as-received 304SS specimens. The Cr enrichment is observed near grain boundaries and the degree of Cr enrichment is different from boundary to boundary.

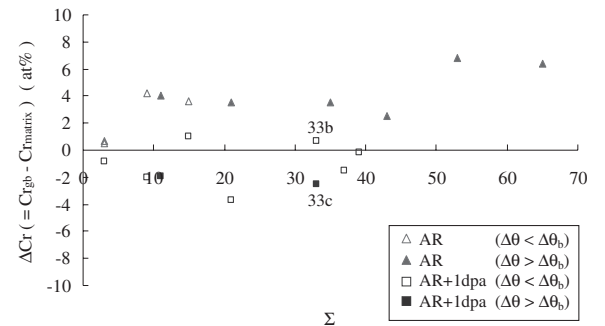


Fig. 5 The segregation levels of Cr atoms ($\Delta Cr \equiv Cr_{gb} - Cr_{matrix}$) at boundaries of different Σ value for both AR and AR + 1 dpa specimens. All the boundaries are not exact CSL boundaries, rather they have deviations from CSL structures. Here, we label a boundary by the nearest Σ .

label a boundary by the nearest Σ . The white triangles(squares) refer to as-received(irradiated) grain boundaries with $\Delta\theta < \Delta\theta_b$, where, according to the Brandon criterion, $\Delta\theta_b = 15^\circ/\sqrt{\Sigma}$. The black ones refer to the boundaries with $\Delta\theta > \Delta\theta_b$, and boundaries of these kinds are regarded as random boundaries here.

In Fig. 5, for AR specimens we can see that the Cr enrichment levels at boundaries of higher Σ value (here, $\Sigma = 53$ or 65) are higher than those at CSL boundaries, and almost no Cr enrichment is found at $\Sigma 3$ boundaries. After irradiation to 1 dpa at 450°C , the Cr profiles across grain boundaries are changed. Most of the boundaries show slight Cr depletion, but some remain Cr enrichment of a small amount. This suggests that initially Cr-enrichment appears to delay subsequent radiation induced Cr depletion at grain boundaries, as reported by other workers,²³⁾ and that the delay is different from boundary to boundary. In general, the $\Sigma 3$ boundaries have least enrichment and depletion due to their more order structures, and the random boundaries have higher enrichment and depletion levels due to their more open structures.

3.2 SEN and SEN + 1 dpa specimens

The representative concentration profiles across grain boundary are shown in Fig. 6 for both the SEN and SEN + 1 dpa 304SS specimens. We can see from Fig. 6 that, for sensitized specimens, depletion of Cr and enrichment of Fe at grain boundaries are observed clearly, and for irradiated sensitized specimens, depletion of Cr and Fe and enrichment of Ni and Si at grain boundaries are observed after irradiation. The concentration profiles of Fe, Cr and Ni near grain boundary after irradiation are superposed on those before irradiation. The RIS effect which occurred in the initially sensitized specimens during irradiation can be

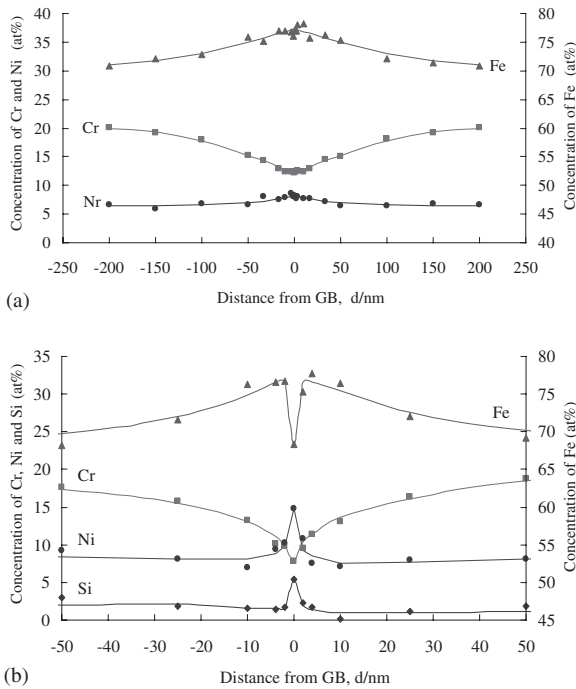


Fig. 6 The representative concentration profiles across grain boundary for both the (a) SEN and (b) SEN + 1 dpa 304SS specimens.

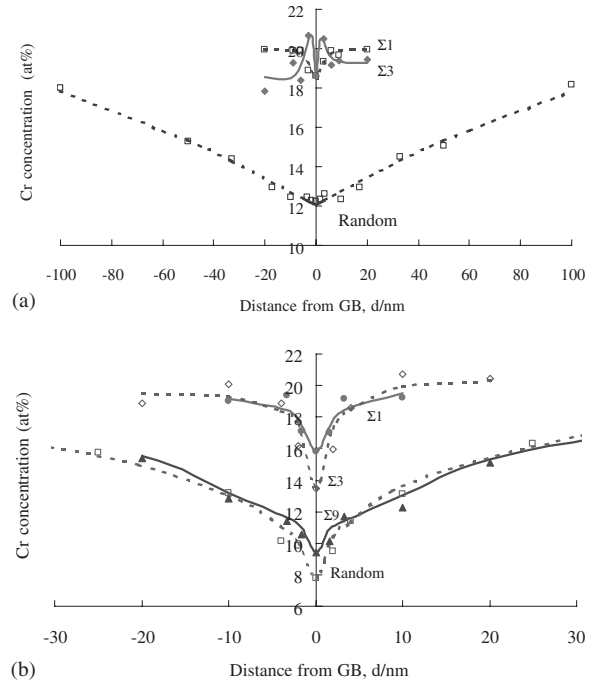


Fig. 7 The Cr concentration profiles across grain boundaries of different Σ value in both the (a) SEN and (b) SEN + 1 dpa 304SS specimens. The degree of Cr depletion is different from boundary to boundary for both the SEN and SEN + 1 dpa specimens.

observed clearly in the irradiated sensitized specimens.

Figure 7 plots the Cr concentration profiles across grain boundaries of different Σ value in both the SEN and SEN + 1 dpa 304SS specimens. As can be seen, the degree of Cr depletion is different from boundary to boundary for both the SEN and SEN + 1 dpa specimens. Normally, the Cr depletion levels at random boundaries are deeper than those at special boundaries, and for $\Sigma 3$ and low angle boundaries only slight Cr depletion is observed (compared with random boundaries). The depletion levels of Cr atoms ($\Delta\text{Cr} \equiv \text{Cr}_{\text{gb}} - \text{Cr}_{\text{matrix}}$) at boundaries of different Σ are shown in Fig. 8 for both SEN and SEN + 1 dpa 304SS specimens. From Fig. 8 we may see that (a) the Cr depletion level at CSL boundary

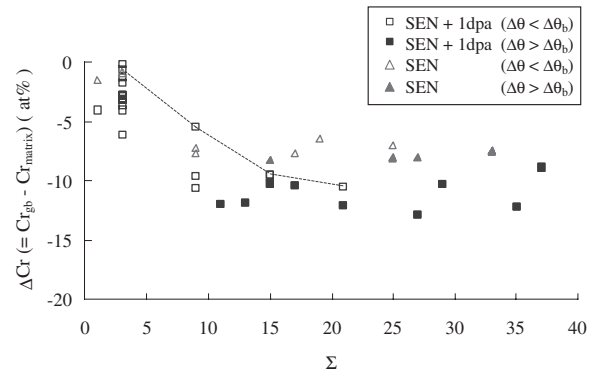


Fig. 8 The depletion levels of Cr atoms ($\Delta\text{Cr} \equiv \text{Cr}_{\text{gb}} - \text{Cr}_{\text{matrix}}$) at boundaries of different Σ for both SEN and SEN + 1 dpa 304SS specimens. It may be seen that (a) the Cr depletion level at CSL boundary increases with Σ for $\Sigma \leq 21$ in SEN + 1 dpa specimens (as shown with dotted line), (b) the Cr depletion level varies with $\Delta\theta$ for the boundaries of the same Σ .

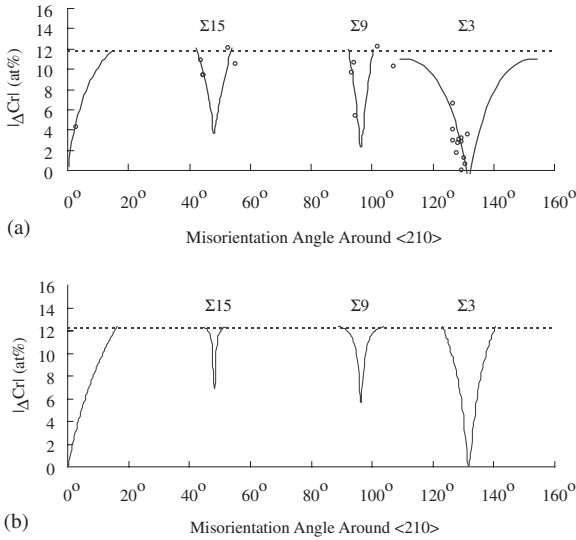


Fig. 9 The variations in Cr segregation levels at grain boundaries of different Σ value as a function of misorientation angles with rotation axis (210) for sensitized irradiated 304 stainless steels. Both of the (a) measured and (b) calculated results indicate the trends that the Cr segregation levels at special boundaries are increasing with Σ .

increases with Σ for $\Sigma \leq 21$ in SEN + 1 dpa specimens (as shown with dotted line), and (b) the Cr depletion level varies with $\Delta\theta$ (misorientation angle from the exact CSL) for the boundaries of the same Σ .

Furthermore, to see the dependence of ΔCr on $\Delta\theta$ for the SEN + 1 dpa specimens, we plot the variations in depletion levels of Cr with misorientation angle with rotation axis (210), as shown in Fig. 9(a). In Fig. 9(a), the small circles are measured points, and the solid lines are obtained by curve fitting. We can see from the fitted curves that three cusps appear at $\Sigma 3$, $\Sigma 9$ and $\Sigma 15$ boundaries, and the Cr depletion levels at CSL boundaries is also increasing with Σ for values up to $\Sigma = 15$. In doing the above curve fitting, we have assumed that the shape of the segregation cusp is similar to that of the boundary energy cusp. For further details, please refer to our previous work.¹⁷⁾

From the results of the experiments, it is certain that the grain boundary segregation is related to the grain boundary structures. The degree of grain boundary segregation is dependent upon the grain boundary misorientation, Σ and $\Delta\theta$.

4. Program Simulation and Comparison with Experimental Results

4.1 Model description

In this section, we'll develop a model to describe the effects of grain boundary segregation on radiation induced segregation (RIS) in irradiated 304 stainless steels. In order to describe the structures of grain boundary, the grain boundary dislocation model will be used here. We'll consider, for simplicity, a pure symmetric tilt boundary consisting of an array of parallel edge dislocations, which are primary dislocations for low-angle boundary, or secondary dislocations for singular or vicinal high-angle boundary. Normally, most of the diffusing defects from the bulk would impinge

upon the boundary surface and then diffuse along the grain boundary to the grain boundary dislocations which will be assumed to be perfect sinks for defects. Therefore, the model to be developed will be based on the RIS model along with grain boundary diffusion and grain boundary dislocation model.

4.1.1 RIS model with modified boundary conditions

The RIS model used here for Fe-Cr-Ni alloys is based on the Lam *et al.*'s model.²⁴⁾ The rate equations of atoms (Fe, Cr and Ni) and defects (vacancy and interstitial) are

$$\begin{aligned}\frac{\partial C_v}{\partial t} &= -\nabla \cdot J_v + \eta K_0 - RC_v C_i, \\ \frac{\partial C_i}{\partial t} &= -\nabla \cdot J_i + \eta K_0 - RC_v C_i, \\ \frac{\partial C_k}{\partial t} &= -\nabla \cdot J_k \quad (k = \text{Cr, Ni or Fe}).\end{aligned}\quad (1)$$

C_k , C_v and C_i are the concentrations of each atom, vacancy and interstitial, respectively. J_v , J_i and J_k are the fluxes of the vacancy, interstitial and atoms, and R and ηK_0 are the recombination coefficient and the effective damage rate, respectively.

Usually, the initial conditions for the rate equations are (a) thermal equilibrium defect concentrations and (b) uniform composition of the alloy throughout. The boundary conditions at the grain boundaries for the atoms are $J_k = 0$ because of conservation of atoms in a closed system, and for the defects are generally taken as equal to the thermal equilibrium concentrations if the grain boundaries are perfect sinks. For actual grain boundaries, however, the thermal equilibrium defects concentrations may not be maintained in their vicinities due to the lower sink efficiency of the boundaries. The boundary conditions for defects at actual boundaries should be modified here.

To modify the boundary conditions for defects at boundaries, we consider the rate equations for defects in a region of the lattice directly adjacent to the boundary, as shown in Fig. 10. The rate equation of vacancy near boundary may be written as

$$\Delta x \frac{\partial C_v}{\partial t} = J_v^1 - J_v^0 + \Delta x \eta K_0 - \Delta x RC_v C_i, \quad (2)$$

where J_v^1 and J_v^0 are the fluxes of vacancies flowing into and out of the region directly adjacent to the boundary, respectively. The vacancies leaving the directly vicinal region, for high-angle boundary, are assumed to diffuse along the grain boundary to the secondary grain boundary dislocations, and for low-angle boundary are assumed to diffuse directly to the primary grain boundary dislocations. The grain boundary dislocations, due to assumed to be perfect sinks, can maintain the concentration of defects in its direct vicinity at its local equilibrium value, C_v^{eq} .

Furthermore, the flux J_v^0 may be related to J_v^{gb} , the flux flowing along the boundary, by

$$J_v^0 = 2J_v^{\text{gb}} \delta(b/d)(1/b) = 2J_v^{\text{gb}} \delta(2/b) \sin(\Delta\theta/2) \quad (\text{for high-angle GB, and } J_v^{\text{gb}} \text{ in unit of cm}^{-2}), \quad (3a)$$

$$J_v^0 = J_v^{\text{gb}} (b/d)(1/b) = J_v^{\text{gb}} (2/b) \sin(\theta/2) \quad (\text{for low-angle GB, and } J_v^{\text{gb}} \text{ in unit of cm}^{-1}), \quad (3b)$$

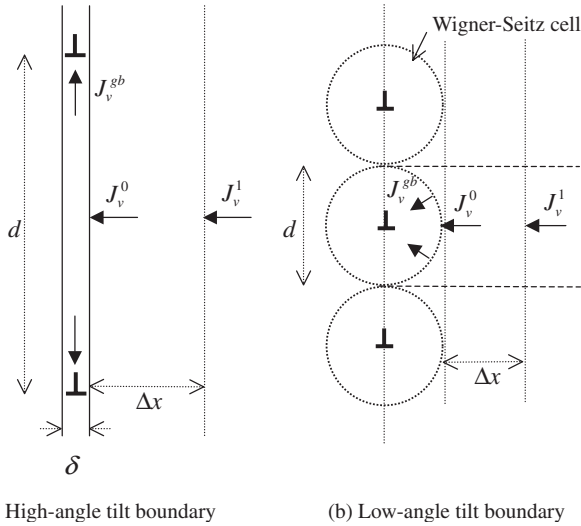


Fig. 10 Diagrams of modified boundary conditions for defects at grain boundaries in RIS model. (a) The defects impinging upon the high-angle grain boundaries through a cross section of $1 \times d$ will diffuse along boundaries through a cross section of $1 \times \delta$ to dislocations where defects absorbed. (b) The defects will diffuse directly to the grain boundary dislocations in low-angle boundaries.

where d and δ are the mean spacing of grain boundary dislocations and boundary thickness, respectively. J_v^1 can be expressed in terms of the concentrations near boundary by diffusion equation. In eq. (3a), b is the Burgers vector of the secondary grain boundary dislocations and $\Delta\theta$ is the deviation angle from exact CSL boundary ($\Delta\theta = \theta - \theta_{\text{CSL}}$), and in eq. (3b), b is the Burgers vector of the primary grain boundary dislocations and θ is the misorientation angle.

Since the vacancies can jump via Fe, Cr or Ni in the boundary, the vacancy flux along boundary can be written as

$$J_v^{\text{gb}} = \sum J_{vk}^{\text{gb}} \quad (k = \text{Fe, Cr and Ni}), \quad (4)$$

where J_{vk}^{gb} is the flux of vacancies via k atoms in the boundary. J_{vk}^{gb} is assumed to have the form as

$$J_{vk}^{\text{gb}} = S d_{vk}^{\text{gb}} C_k (C_v - C_v^{\text{eq}}), \quad (5)$$

where S is the sink strength of the grain boundary dislocations and d_{vk}^{gb} is the diffusivity coefficients for vacancy-atom pairs vk in the boundary. The sink strength S may be written as a product of three parameters,¹⁶⁾ in the form

$$S = g_0 z m, \quad (6)$$

where g_0 is a purely geometrical parameter, z is the sink capture efficiency and m is a multiple sink correction factor. The geometrical parameter, g_0 , for the sink of grain boundary dislocations is $g_0 = 1/(\frac{d}{2} - r_0)$ for high-angle boundaries and $g_0 = \pi/\ln(\frac{d}{2r_0})$ for low-angle boundaries,¹⁶⁾ r_0 is the radius of the grain boundary dislocations, here we set $r_0 = \alpha b$, b is the Burgers vector of grain boundary dislocation and α is a constant of the order of unity.¹⁵⁾ The parameter z is defined as the ratio of the actual point defect current to the sink to the corresponding current which would result if the sink were perfect. In our case, $z = 1$ for grain boundary dislocations which are assumed to be perfect sinks. The parameter m accounts for the interactions between sinks when many sinks are present. We'll ignore the interactions between grain

boundary dislocations, so $m = 1$ here.

The diffusivity coefficients in the boundaries may be written as¹⁵⁾

$$d_{vk}^{\text{gb}} = g_v a^2 Z_v f_v^{\text{gb}} (v_{vk})_0 \exp\left(-\frac{E_{vk}^{\text{m}}}{kT}\right). \quad (7)$$

Here, g_v is a dimensionless constant depending on the structure, a is the lattice constant, Z_v the coordination number, f_v^{gb} the correlation factor, $(v_{vk})_0$ the vibrational frequency (including entropy term), and E_{vk}^{m} the migration energy for diffusion of a vacancy via k atom in the boundaries. We assume that $(v_{vk})_0$ in the boundaries has the same value as that in the bulk, and take $f_v^{\text{gb}} = 0.5$.²⁵⁾ If the energies of the activated state in diffusion are approximately the same for the boundary and bulk, the migration energies of the grain boundary and bulk diffusion may be related to grain boundary energy (γ) by the expression²⁶⁾

$$E_{vk}^{\text{m}} \approx E_{vk,\text{bulk}}^{\text{m}} - \frac{a^2}{n} \gamma \quad (8)$$

where n is the thickness of a boundary expressed in terms of the number of atomic layers. We'll take $n = 1$ here.²⁷⁾

Finally, J_v^0 can be written as

$$J_v^0 = 4 f_v^{\text{gb}} S \frac{\delta}{b} \sin\left(\frac{\Delta\theta}{2}\right) [D^{\text{bulk}}] \times \exp\left(\frac{a^2 \gamma}{kT}\right) (C_v - C_v^{\text{eq}}) \quad (\text{for high-angle GB}), \quad (9)$$

where $[D^{\text{bulk}}]$ is a quantity related to the diffusion in bulk and would be the same order as that of the diffusion coefficient in bulk. With eqs. (2) and (9), we may have a new boundary condition for defects at grain boundaries instead of boundary condition of thermal equilibrium concentration. The new boundary condition will depend on the quantities of grain boundary, such as density of grain boundary dislocations and grain boundary energy. Similarly, the boundary conditions for the flux of interstitials at grain boundaries can be obtained.

4.1.2 Burgers vectors of grain boundary dislocations

In eq. (9), b is the Burgers vector of the secondary grain boundary dislocation. For high-angle boundary, the reference lattice of the grain boundary is a DSC-Lattice. The primitive Burgers vectors of the secondary grain boundary dislocations are defined by the basis vectors of the DSC lattice. The basis vectors of the DSC lattice for boundaries of different Σ in FCC crystals are listed in Table 1.²⁸⁾ The three basis vectors of DSC lattice have been multiplied by 2Σ , in order to avoid the use of fractional indices. It can be seen from Table 1 that the magnitude of the primitive Burgers vectors decreases, on average, with increasing Σ because the DSC lattice is related to the reciprocal lattice of the CSL. It is expected that for any grain boundary the most likely existing Burgers vectors of the infinity of possible Burgers vectors will be associated with a lower energy than any other, and this is expected to be the Burgers vector with the smallest length. Besides, for a symmetric tilt boundary, the Burgers vector of the grain boundary dislocations should be perpendicular to tilt axis. The Burgers vectors, which are both most likely existing and perpendicular to tilt axis, are also listed in the latter two

Table 1 Basis vectors of the DSC lattice for FCC crystals.

Σ	$2\Sigma b_x$	$2\Sigma b_y$	$2\Sigma b_z$	$b_{\min} \perp \langle 110 \rangle$	$b_{\min} \perp \langle 210 \rangle$
3	2 2 2	$\bar{1}$ 2 $\bar{1}$	$\bar{1}$ $\bar{1}$ 2	$b_y + b_z$	$b_y + b_z$
5	0 3 1	0 $\bar{1}$ 3	5 $\bar{1}$ $\bar{2}$		
7	2 1 $\bar{3}$	$\bar{1}$ 3 $\bar{2}$	5 6 3		b_x
9	1 $\bar{1}$ 4	$\bar{4}$ 4 2	3 6 3	b_x	b_y
11	$\bar{3}$ 3 2	2 $\bar{2}$ 6	7 4 $\bar{1}$	b_x	
13a	0 5 1	0 1 $\bar{5}$	13 2 3		
13b	$\bar{3}$ $\bar{1}$ 4	1 4 3	8 7 11		
15	1 $\bar{2}$ 5	9 3 0	4 7 5		b_x
17a	0 5 $\bar{3}$	0 3 $\bar{5}$	17 4 1		
17b	4 3 3	$\bar{6}$ 4 4	$\bar{1}$ 12 $\bar{5}$	b_x	
19a	1 $\bar{1}$ 6	6 $\bar{6}$ $\bar{2}$	9 10 $\bar{3}$	b_x	
19b	3 2 $\bar{5}$	$\bar{2}$ 5 $\bar{3}$	13 15 10		
21a	1 $\bar{5}$ 4	4 1 $\bar{5}$	14 14 14		
21b	2 $\bar{8}$ 4	6 3 $\bar{9}$	3 9 6		b_x
23	$\bar{1}$ 6 $\bar{3}$	$\bar{5}$ 7 8	10 9 7		b_x

columns in Table 1.

4.1.3 Grain boundary energies

We can see from eq. (8) that the grain boundary energy is a major contributor to the diffusion fluxes of defects in boundaries. Based on the grain boundary dislocation model, the grain boundary energy can be written as²⁹⁾

$$\gamma = \gamma_0 + \gamma_{\text{core}} + \gamma_{\text{el}}, \quad (10)$$

where γ_0 is the energy per unit area of the reference structure, γ_{core} is the core energy of the grain boundary dislocations per unit area of the boundary and γ_{el} is the elastic energy per unit area of the boundary associated with the elastic field of the grain boundary dislocations. In general, the core and the elastic energies of the dislocations are mainly confined to the dislocations themselves. In this model, since we are interested in the segregation effects of special boundaries, the diffusion will be focused mainly on the area of the reference structure. Therefore, for simplicity, it is assumed that the energy of grain boundary is mainly from that of the reference structure and the core and elastic energies of grain boundary dislocations are ignored.

In CSL model, the boundaries with lower Σ value would have better matching structure than those with higher Σ value. It was shown in Ref. 30), and is adopted here, that the grain boundary energy could be related to Σ by the following expression

$$\gamma = \gamma_b(1 - 1/\sqrt{\Sigma}). \quad (11)$$

Here, γ_b is the energy of “bad” boundaries. We believe γ_b is not just a simple constant, instead it might be dependent on the other properties of grain boundaries, say the inclination of the boundary.

4.2 Model results

The model calculations were performed to evaluate the segregation levels of solute atoms at grain boundaries of different Σ value. The LSODE numerical integration subroutine was used for the rate equations. The input parameters for rate equations were assumed to be the same as used by Allen *et al.*³¹⁾ and were listed in Table 2. So far, the yet determined parameter is the grain boundary energy, γ_b , in eq. (11). It should be determined from the measured free energies of grain boundaries. However, from the experimental data in hand, we cannot accurately determine γ_b at the moment. We can only tell the range where it may lie, *i.e.*, somewhere between 47 and 795 mJ/m². The way to determine γ_b was described in our previous work.¹⁸⁾ Here, we'll take $\gamma_b = 355$ mJ/m² in our model calculations.

Figure 11 shows the calculated Cr concentration profiles across grain boundaries of different Σ value for the SEN + 1 dpa 304SS specimens. In Fig. 11, for simplicity, we assume that the initial concentration profiles (shown as dotted line) are the same for the boundaries of different Σ and take $\Delta\theta = 1^\circ$. In order to compare with the measured composition profiles, we have taken into account the beam broadening effect by a convolution of the calculated composition profile with the X ray generation function which was coming with the broadened electron beam. The model calculations indicate that the degree of Cr depletion is different from boundary to boundary, and that the Cr depletion levels at random boundaries are deeper than those at special boundaries, and increase with Σ value. Compared with Fig. 7(b), we

Table 2 RIS input parameters in this model.

Input parameter	Notation	Value	Refs.
Vacancy jump frequency for Fe	$v_{\text{Fe-v}}^0$	$2.8 \times 10^{13} \text{ s}^{-1}$	32)
Vacancy jump frequency for Cr	$v_{\text{Cr-v}}^0$	$5.0 \times 10^{13} \text{ s}^{-1}$	32)
Vacancy jump frequency for Ni	$v_{\text{Ni-v}}^0$	$1.5 \times 10^{13} \text{ s}^{-1}$	32)
Interstitial jump frequency for Fe, Cr and Ni	$v_{\text{k-i}}^0$	$1.5 \times 10^{12} \text{ s}^{-1}$	32)
Vacancy migration energy for Fe, Cr and Ni	$H_{\text{k-v}}^m$	1.3 eV	32)
Interstitial migration energy for Fe, Cr and Ni	$H_{\text{k-i}}^m$	0.9 eV	32)
Vacancy formation energy	H_v^f	1.9 eV	32)
Interstitial formation energy	H_i^f	4 eV	33)
Fe-vacancy correlation factor	f_{Fev}	0.785	32)
Cr-vacancy correlation factor	f_{Crv}	0.668	32)
Ni-vacancy correlation factor	f_{Niv}	0.872	32)
Atom-interstitial correlation factor	f_i	0.44	32)
Vacancy formation entropy	S_v^f	5 k	33)
Interstitial formation entropy	S_i^f	0 k	33)

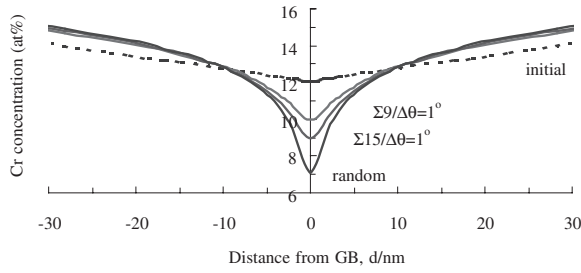


Fig. 11 The calculated Cr concentration profiles across grain boundaries of different Σ value for the SEN + 1 dpa 304SS specimens. It may be seen that the results of model calculations and experiments are similar.

may see that the results of model calculations and experiments are quite similar.

Figure 9(b) displays the model calculations of Cr variations in segregation levels at grain boundaries of different Σ value as a function of misorientation angle for irradiated sensitized 304 stainless steels. In Figs. 9(a) and (b), both of the calculated and measured results indicate the trend that the Cr segregation levels at special boundaries in irradiated 304 stainless steels is increasing with Σ for the lower Σ values. Although not obvious, we can see in Fig. 9(b) that the widths of the cusps also change with Σ value, as implied by the Brandon's criterion.²²⁾ In doing the above model calculations for the irradiated sensitized case, the measured sensitized concentration profiles were taken as the initial profiles for $\Sigma = 9$ and 15 boundaries, but for low-angle and $\Sigma = 3$ boundaries the depths and widths of the initial profiles were assumed to be increasing with misorientation angles. In this model, because the density of the secondary dislocation is zero at $\Delta\theta = 0$, the segregation levels will be estimated to be zero at singular boundaries. Therefore, a small deviation from exact CSL boundary (here, we let $\Delta\theta = 0.1^\circ$) was necessary for comparing the segregation levels at CSL boundaries of different Σ value in Fig. 9(b).

From the model calculations we may see that the RIS model with modified boundary conditions can predict the radiation-induced segregation for grain boundaries with different Σ 's and misorientations, and the results of model calculations are quite consistent with those of experiments.

5. Discussions

5.1 As-received and as-received with irradiation

From the results of AR + 1 dpa specimens, a delay of Cr depletion at grain boundaries was observed. During irradiation, the Cr atoms initially enriched at grain boundaries will diffuse away from the boundary due to pre-existing concentration gradient and inverse Kirkendall effect. In our case, it seems that, after irradiation for 1 dpa at 450°C, the pre-existing concentration gradient has dispersed for most of the grain boundaries. We may say that the radiation induced Cr depletion is occurring with a 1 dpa delay compared with no pre-enrichment condition. We can see from Fig. 5 that the delay is different from boundary to boundary, however we could not find any correlations between grain boundary segregation and misorientation in AR + 1 dpa 304SS specimens. This might be attributed to that random bounda-

ries normally have higher Cr enrichment level than CSL boundaries do in AR specimens, and after irradiation, the RIS effect is stronger on random boundaries than CSL boundaries. Therefore, it appears that there is no obvious correlation between grain boundary segregation and misorientation in irradiated 304SS specimens with initially enriched Cr at grain boundaries.

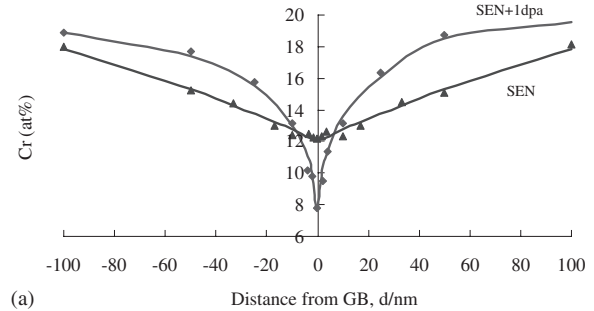
5.2 Sensitized and sensitized with irradiation

Next, we'll describe the effects of pre-sensitization on RIS at boundaries with different $\Delta\theta$. For random boundaries in SEN + 1 dpa specimens, we can see from Fig. 12(a) that the measured Cr concentration profiles after irradiation are changed into narrower and deeper profile as compared with initially thermal sensitized profile. By model calculations for random boundaries with the same initially sensitized profiles, we can obtain the similar profile, as shown in Fig. 12(b). Another calculated profile illustrated in Fig. 12(b) is a Cr concentration profile of an irradiated CSL boundary of $\Sigma 9$. We may see that the Cr concentration at CSL boundary was increasing instead of decreasing after irradiation, if the CSL boundary had the same initially sensitized profiles. This is due to the fact that the degree of RIS effect is usually small at CSL boundaries.

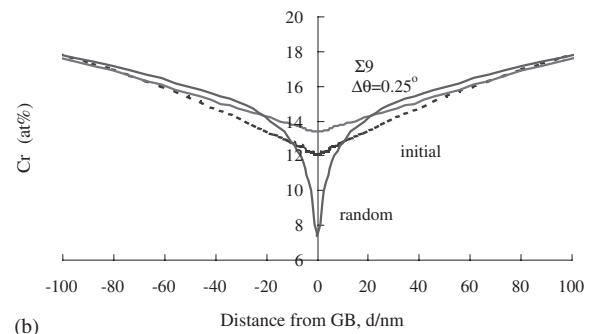
During irradiation, the flux equation for solute atom k is given by

$$J_k = -D_k \alpha \nabla C_k + d_{kv} C_k \nabla C_v - d_{ki} C_k \nabla C_i,$$

where $D_k = d_{kv} C_v + d_{ki} C_i$. The flux of solute atoms includes the concentration gradient flux and the inverse Kirkendall



(a)



(b)

Fig. 12 (a) The measured and (b) the model calculated Cr concentration profiles across grain boundaries in both SEN and SEN + 1 dpa 304 SS. After irradiation, the Cr concentration profile at random boundaries changes to narrower and deeper profile compared with thermal sensitized profile. However, for CSL boundaries, the Cr concentration is increasing instead of decreasing.

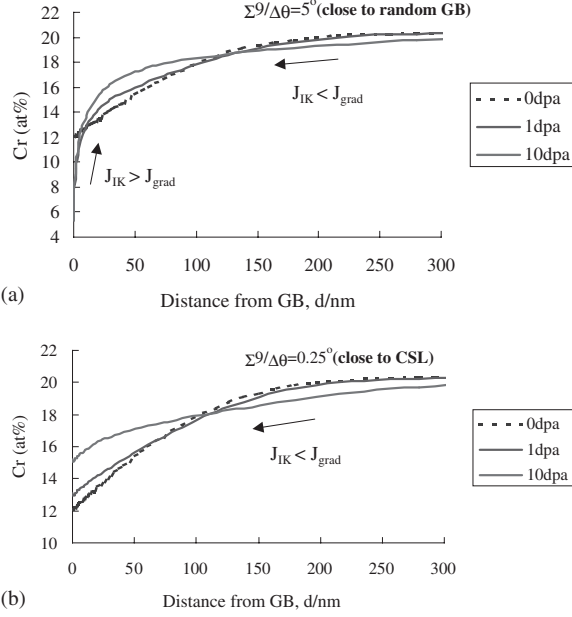


Fig. 13 The evolutions of concentration profiles of Cr with dose for (a) random boundaries, and (b) CSL boundaries. For random boundaries, the profiles go narrower as doses increase, however, for CSL boundaries, the profiles go wider as doses increase.

flux. In the specimens with a pre-existing Cr depletion profile due to thermal sensitization, the concentration gradient flux will compete with the inverse-Kirkendall flux during irradiation. If the inverse-Kirkendall flux is greater than the concentration gradient flux near grain boundaries, Cr will be further depleted at grain boundaries after irradiation. In a region away from grain boundary where the concentration gradient flux exceeds the inverse-Kirkendall flux, Cr will move toward the grain boundary. Finally, Cr will accumulate in a region between areas near and far away from boundary, and hence result in a narrower Cr profile than initial one as shown in Fig. 13(a). The evolutions of concentration profiles of Cr with dose are also shown in Fig. 13. For random boundaries, the profiles go narrower as increase in dose. However, for CSL boundaries, the profiles go wider as increase in dose, as shown in Fig. 13(b). This is due to that the RIS effect is usually small at CSL boundaries. Therefore, the concentration gradient flux exceeds the inverse-Kirkendall flux even in a region near grain boundary, and the net flow of Cr atom will be in the direction of grain boundary for CSL boundary during irradiation. Actually, the recovery of chromium concentration profile near CSL boundaries in irradiated sensitized specimens is caused by its chemical gradient, and also affected by radiation-enhanced diffusion via irradiation-introduced point defects.

5.3 RIS model with modified boundary conditions

The RIS model with modified boundary conditions, which are related to the grain boundary diffusion of defects and the densities of the grain boundary dislocations, was developed for boundaries of different Σ value. In the conventional RIS model, the grain boundaries are generally treated as perfect sinks, and the boundary condition for defects at the grain boundaries is $C_v = C_v^{eq}$. In the modified RIS model, it is the

random boundary that behaves as perfect sink. Hence, the boundary condition for defects at the random boundaries will be $C_v = C_v^{eq}$ too, as described below.

At early times during irradiation, J_v^0 is approximately equal to zero because C_v at grain boundaries is close to C_v^{eq} in eq. (9). As time goes on, J_v^0 along with C_v is increasing with time till $\partial C_v / \partial t = 0$. At steady state, J_v^0 is balanced off by the rest terms, $J_v^1 + (\eta K_0 - RC_v C_i) \Delta x$, on the right-hand side of eq. (2). Hence, the equilibrium defect concentrations at grain boundaries may be determined from eqs. (2) and (9) at steady state. For random boundaries, the diffusivity coefficient, d_{vk}^{eq} , in boundaries is a very large value compared to that in bulk, for instance, for energy of random boundary in 304SS ($\gamma = 790 \text{ mJ/m}^2$), $\exp(\gamma/kT) \approx d_{vk}^{eq}/d_{vk} \approx 3.7 \times 10^4$ at 450°C . J_v^0 would become so a large value due to a small increasing in C_v from C_v^{eq} that the random boundaries would absorb the defects very rapidly and behave as perfect sinks. In this model, therefore, for random boundaries the equilibrium defect concentration at steady state is very close to that in thermal equilibrium. We may say that this model can go back to the conventional RIS model if the grain boundary is a random boundary.

For special boundaries, the diffusing fluxes on boundaries are smaller than those on random boundaries due to the facts that the energies of special boundaries are lower than those of random boundaries. To increase the diffusing fluxes on special boundaries for reaching steady states during irradiation, the defect concentrations at grain boundaries need to be higher than those at random boundaries. Therefore, the defect concentration at special boundaries at steady state is higher than thermal equilibrium value, as can be seen from eq. (9), and this value is dependent upon the energies and the misorientation angles of the grain boundaries.

From the results of the experiments, it can be seen that the degree of grain boundary segregation is dependent upon the grain boundary misorientation, Σ and $\Delta\theta$, which in turn is related to the grain boundary energy and the density of grain boundary dislocations. For low-angle boundaries, the degree of segregation increases with misorientation (θ), and this can be attributed to the increase in primary dislocation density with misorientation. For high-angle boundaries, the segregation cusps are observed at special boundaries. When deviated from the exact CSL boundary, the segregation levels will also increase with the misorientation ($\Delta\theta = \theta - \theta_{CSL}$), and similarly this can also be attributed to the increase in the density of secondary grain boundary dislocations with misorientation.

Besides, segregation levels will depend upon the magnitude of diffusing defect fluxes on boundaries, the diffusing defect fluxes in turn depend upon the grain boundary energies. Figure 14 plots the predicted segregation levels of Cr at boundaries with different energies for as-received 304 stainless steels with 1 dpa irradiation. It can be also seen that the predicted segregation levels of Cr at CSL boundaries are increasing with Σ for boundaries with the same initially uniform concentrations over the bulk, and that for each CSL boundary the segregation levels of Cr increase with energy. Actually, in our model the Cr segregation levels at special boundaries will be increasing with Σ if we adopt the assumption that the grain boundary energy could be related to

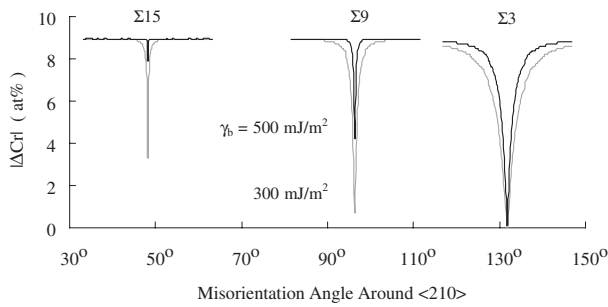


Fig. 14 The predicted segregation levels of Cr at boundaries with different energies for as-received 304 stainless steels with 1 dpa irradiation. It can be also seen that the predicted segregation levels of Cr at CSL boundaries are increasing with Σ , and that for each CSL boundary the segregation levels of Cr increase with energy.

Σ by eq. (11). So far, we have not considered the factor of the inclination of the boundary in our model. The grain boundary energy is known to be dependent on the boundary inclination.¹⁵⁾ In many situations, boundaries migrate locally in order to change their inclination and reduce their energy. In this model it could be possible that the parameter γ_b in eq. (11) is related to the inclination of the boundary.

The large-angle boundaries act as sinks more readily via the climb of secondary dislocations in the boundary plane. For boundaries near CSL structure, the density of intrinsic secondary dislocations is low (or zero as in singular boundary), the segregation level is calculated to be close to zero in this model. In real situation, however, a sufficient density of extrinsic dislocations may be produced to dominate the kinetics.¹⁵⁾ This may occur as a result of the impingement of lattice dislocations on the boundaries. The segregation level may not be zero at an initially singular boundary.

This model was shown to predict the radiation-induced segregation for grain boundaries of different energies and misorientation. However, there are some limitations in this model as described below. Some of the input parameters used on grain boundary, which are not available for this moment, were assumed to be the same as those used in bulk, and this may not be the truth. Especially, the grain boundary energies for special boundaries of different Σ 's in 304 stainless steels are not available from measurements or theoretical calculations, except $\Sigma 3$ boundaries. Dislocations were treated as ideal sinks for defect fluxes in this model. Actually, the absorption of defects at the dislocation lines is a complex process¹⁵⁾ which involves the jumping of defects into the core, the diffusion of these defects along the core to jogs, and the nucleation of jog pairs. For further details on the sink efficiency of dislocations please refer to the reference 15). The elastic fields of dislocations and boundaries were also neglected in this model. They are local fields and confined to dislocations within the range of few Burgers vectors. When misorientation angle is small, the distance between grain boundary dislocations is large so that any effects of the stress field are relatively small and can be neglected. However, for large misorientation angle, the stress field may overlap each other and may not be negligible.

6. Summary

In this paper, the effects of grain boundary misorientation on grain boundary segregation were described for specimens of as-received, irradiated, sensitized and irradiated sensitized 304SS. A simple rate equation model with modified boundary conditions, which include the fluxes of defects diffusing along the grain boundaries to the grain boundary dislocations, was developed for RIS at boundaries of different Σ value. The results of the experiments and model calculations are summarized as follows:

- (1) From the results of the experiments, it is certain that the grain boundary segregation is related to the grain boundary structures. The degree of grain boundary segregation is dependent upon the grain boundary misorientation, Σ and $\Delta\theta$.
- (2) For the as-received specimens with enriched Cr at grain boundaries, a delay compared with no pre-enrichment of Cr depletion at grain boundaries was observed after 1 dpa irradiation at 450°C. And for the sensitized specimens after irradiation, the Cr concentration profile becomes narrower and deeper than that of the SEN specimens.
- (3) The segregation cusps were found at the $\Sigma 3$ boundaries for all of the specimens of AR, SEN and irradiated types. Therefore, the $\Sigma 3$ boundary is a very special boundary which has good resistance to solute segregation.
- (4) From the results of model calculations, we see that the RIS model with modified boundary conditions can predict the radiation-induced segregation for grain boundaries of different Σ 's and misorientations. The results of model calculations are quite consistent with those of experiments.
- (5) Both of the calculated and measured results indicate the trends that the Cr segregation levels at special boundaries in irradiated 304 stainless steels are increasing with Σ for the lower Σ values.

Acknowledgements

This study was supported by Center of Electron Microscopy for FEGTEM/EDS observation and Van de Graaff Accelerator Center for proton irradiation in National Tsing Hua University.

REFERENCES

- 1) G. S. Was and P. Andresen: *J. Metals* **44** (1992) 8-13.
- 2) W. C. Johnson and J. M. Blakely: *Interfacial Segregation*, (American Society for Metals, Metals Park, OH, 1979) pp. 450-432.
- 3) P. R. Okamoto and L. E. Rehn: *J. Nucl. Mater.* **83** (1979) 2-23.
- 4) A. Otsuki and M. Mizuno: *Proceedings of JIMIS-4*, Transactions of Japan Institute of Metals (Suppl.) **27** (1986) pp. 789-803.
- 5) F. S. Chen and A. U. King: *Acta Metall.* **36** (1988) 2827-2839.
- 6) H. Mykura: *Grain Boundary Structure and Kinetics*, (American Society for Metals, Metals Park, OH, 1980) pp. 209-238.
- 7) T. Watanabe: *J. de Physique* **46** (1985) c4-555-c-566.
- 8) C. L. Briant: *Acta Metall.* **31** (1983) 257-266.
- 9) T. M. Devine: *J. Mater. Sci.* **32** (1997) 1555-1562.
- 10) M. S. Laws and P. J. Goodhew: *Acta Metall. Mater.* **39** (1991) 1525-1533.

- 11) T. S. Duh, J. J. Kai, F. R. Chen and L. H. Wang: J. Nucl. Mater. **258-263** (1998) 2064-2068.
- 12) A. P. Sutton and R. W. Balluffi: *Interfaces in Crystalline Materials*, (Clarendon, Oxford, 1995) pp. 70-86.
- 13) W. C. Johnson and J. M. Blakely: *Interfacial Segregation*, (American Society for Metals, Metals Park, OH, 1979) pp. 193-237.
- 14) A. P. Sutton and R. W. Balluffi: *Interfaces in Crystalline Materials*, (Clarendon, Oxford, 1995) pp. 606-614.
- 15) A. P. Sutton and R. W. Balluffi: *Interfaces in Crystalline Materials*, (Clarendon, Oxford, 1995) pp. 614-621.
- 16) F. V. Nolfi, Jr.: *Phase Transformation During Irradiation*, (Applied Science, London, 1983) pp. 147-188.
- 17) T. S. Duh, J. J. Kai and F. R. Chen: J. Nucl. Mater. **283-287** (2000) 198-204.
- 18) T. S. Duh, J. J. Kai, F. R. Chen and L. H. Wang: J. Nucl. Mater. **294** (2001) 267-273.
- 19) F. R. Chen and A. H. King: J. Electron Microscopy Techn. **6** (1987) 55-61.
- 20) H. Mykura: *Grain Boundary Structure and Kinetics*, (American Society for Metals, Metals Park, OH, 1980) pp. 445-456.
- 21) V. Randle and B. Ralph: J. Mater. Sci. **21** (1986) 3823-3828.
- 22) D. G. Brandon: Acta Metall. **14** (1966) 1479-1484.
- 23) E. P. Simonen and S. M. Bruemmer: Proceedings of the Eighth International Symposium on Environmental Degradation of Materials in Nuclear Power System - Water Reactors Vol. 2 (1997) pp. 751-757.
- 24) N. Q. Lam, A. Kumar and H. Wiedersich: *Effects of Radiation on Materials, Eleventh Conf., ASTM STP 782* ed. by H. R. Brager and J. S. Perrin, (American Society for Testing and Materials, 1982) pp. 985-1007.
- 25) G. E. Murch and A. S. Nowick: *Diffusion in Crystalline Solids*, (Academic Press, Orlando FL, 1984) pp. 319-377.
- 26) A. N. Aleshin, B. S. Bokshtein and L. S. Shvindlerman: Sov. Phys. Solid State **19** (1977) 2051-2054.
- 27) V. T. Borisov, V. M. Golikov and G. V. Scherbedinskiy: Fiz. Metal. Metalloved. **17** (1964) 881-885.
- 28) A. H. King: Acta Metall. **30** (1982) 419-427.
- 29) D. Schwartz, P. D. Bristowe and V. Vitek: Acta Metall. **36** (1988) 675-687.
- 30) A. N. Aleshin, V. Yu. Aristov, B. S. Bokshtein and L. S. Shvindlerman: Phys. Status Solidi (a) **45** (1978) 359-366.
- 31) T. R. Allen, G. S. Was and E. A. Kenik: J. Nucl. Mater. **244** (1997) 278-294.
- 32) T. R. Allen and G. S. Was: Acta Mater. **46** (1998) 3679-3691.
- 33) A. M. Yacout, N. Q. Lam and J. F. Stubbins: Nucl. Instr. Meth. B **42** (1989) 49-60.